




## PAPER

[View Article Online](#)  
[View Journal](#) | [View Issue](#)Cite this: *Nanoscale Adv.*, 2020, 2, 5841Size and morphology effects on the high pressure behaviors of  $\text{Mn}_3\text{O}_4$  nanorods†Juanying Li,<sup>a</sup> Bo Liu,<sup>a</sup> Junyan Dong,<sup>a</sup> Chenyi Li,<sup>a</sup> Qing Dong,<sup>a</sup> Tao Lin,<sup>a</sup> Ran Liu,<sup>a</sup> Peng Wang,<sup>a</sup> <sup>a</sup> Pengfei Shen,<sup>b</sup> Quanjun Li <sup>\*a</sup> and Bingbing Liu <sup>\*a</sup>

The high-pressure behaviors of  $\text{Mn}_3\text{O}_4$  nanorods were studied by high pressure powder synchrotron X-ray diffraction and Raman spectroscopy. We found that the initial hausmannite phase transforms into the orthorhombic  $\text{CaTi}_2\text{O}_4$ -type structure, and then to the marokite-like phase upon compression. Upon decompression, the marokite-like phase is retained at the ambient pressure. Compared with  $\text{Mn}_3\text{O}_4$  bulk and nanoparticles,  $\text{Mn}_3\text{O}_4$  nanorods show obviously different phase transition behaviors. Upon compression, the phase transition sequence of  $\text{Mn}_3\text{O}_4$  nanorods is similar with the nanoparticles, while the decompression behavior is consistent with the bulk counterparts. The hausmannite phase shows higher stability and smaller bulk modulus in  $\text{Mn}_3\text{O}_4$  nanorods than those of the corresponding bulk and nanoparticles. We proposed that the higher phase stability and compressibility of the nanorods are concerned with their nanosize effects and the rod morphology. Both the growth orientation and the suppressed Jahn–Teller distortion of the  $\text{Mn}_3\text{O}_4$  nanorods are crucial factors for their high pressure behaviors.

Received 26th July 2020  
Accepted 26th October 2020

DOI: 10.1039/d0na00610f

[rsc.li/nanoscale-advances](http://rsc.li/nanoscale-advances)

## Introduction

High-pressure research on nanomaterials has attracted wide attention because of the emergence of many exceptional behaviors of nanocrystals under high pressure.<sup>1–6</sup> Previous research has revealed that the high-pressure behaviors of nanomaterials are significantly different from that of the bulk counterparts, in which the nanosize and the shape have been considered to be crucial factors.<sup>7–9</sup> Recently, the effects of the nanosize and morphology on the phase transitions have been observed in several nanomaterials.<sup>10–21</sup> For example, the phase transition from the hexagonal 4H to the face-centered cubic (fcc) phase has been observed in Au nanoribbons under high pressure, which is different from the other metals.<sup>22</sup> The increased phase transition pressure and size-dependent phase transition selectivity have been revealed in anatase  $\text{TiO}_2$  nanomaterials.<sup>13,23</sup> Moreover, the shape-tuned phase transition sequences have been reported in  $\text{TiO}_2$  nanowires<sup>24</sup> and ZnS nanorods.<sup>25</sup> Amorphous forms have been achieved *via* the application of high pressure in several nanomaterials, such as PbTe nanoparticles,<sup>3</sup>  $\text{TiO}_2$  nanoparticles<sup>26</sup> and nanoribbons,<sup>19</sup>  $\text{Y}_2\text{O}_3$  nanoparticles,<sup>8</sup> and  $\text{VO}_2$  nanosheets.<sup>27</sup> These studies have

demonstrated that the phase transition behaviors depend on not only the size but also the morphology. But the effects of the nanosize and morphology on the high pressure behaviors are various in different systems.

As one of the typical manganese oxides,  $\text{Mn}_3\text{O}_4$  has attracted a great deal of research interest because of its special physical and chemical properties, which provide wide-spread applications in cataluminescence sensing materials and catalysts.<sup>28,29</sup> For example,  $\text{Mn}_3\text{O}_4$  shows an excellent sensing characteristic for volatile organic compounds.<sup>28</sup> What is more,  $\text{Mn}_3\text{O}_4$  is a binary oxide with the  $\text{AB}_2\text{O}_4$  formula. Previous studies have shown that the spinels with the  $\text{AB}_2\text{O}_4$  molecular formula have important technical applications in superhard materials and magnetic materials.<sup>30,31</sup> The cations A and B are distributed in different positions to form different spinel structures. As a typical spinel with superior physical properties,  $\text{Mn}_3\text{O}_4$  exists in the hausmannite phase with a tetragonally distorted structure under ambient pressure. The structure characteristic is that the  $\text{Mn}^{2+}$  and  $\text{Mn}^{3+}$  ions occupy the center positions of the tetrahedral and octahedral, respectively. And  $\text{MnO}_6$  octahedra are stretched along the [001] orientation resulting from the instability of the  $\text{Mn}^{3+}$  ion, causing the tetragonal structure with space group  $I4_1/amd$ .<sup>32</sup> As for its high-pressure structure, there have been high-pressure studies on bulk  $\text{Mn}_3\text{O}_4$  and  $\text{Mn}_3\text{O}_4$  nanoparticles.<sup>32</sup> It was known that the bulk hausmannite  $\text{Mn}_3\text{O}_4$  transforms into the marokite-like phase above 11.5 GPa, and keeps stable up to 47.3 GPa, while the  $\text{Mn}_3\text{O}_4$  nanoparticles have been found to undergo two phase transitions with a new phase at 14.5–23.5 GPa. The size effects are considered to be

<sup>a</sup>State Key Laboratory of Superhard Materials, College of Physics, Jilin University, No. 2699 Qianjin Street, Changchun 130012, People's Republic of China. E-mail: [liquanjun@jlu.edu.cn](mailto:liquanjun@jlu.edu.cn)

<sup>b</sup>Academy for Advanced Interdisciplinary Studies, Southern University of Science and Technology, Shenzhen, 518055, China

† Electronic supplementary information (ESI) available. See DOI: 10.1039/d0na00610f



a dominant factor causing the abnormal phase transition behaviors between the  $\text{Mn}_3\text{O}_4$  bulk and nanoparticles.<sup>32</sup> However, the phase transitions of  $\text{Mn}_3\text{O}_4$  nanorods have not been reported so far. The influences of the size and morphology on the behaviors of  $\text{Mn}_3\text{O}_4$  nanorods are still unknown. Thus, this inspired us to explore further the phase transitions for the  $\text{Mn}_3\text{O}_4$  nanorods.

In this work, the high pressure behaviors of  $\text{Mn}_3\text{O}_4$  nanorods with diameter 30–50 nm were studied up to 42.3 GPa, using high-pressure powder X-ray diffraction and Raman spectroscopy. Compared with the  $\text{Mn}_3\text{O}_4$  bulk and nanoparticles,  $\text{Mn}_3\text{O}_4$  nanorods show unusual high pressure behaviors, especially in the aspect of mechanical properties. The different high-pressure behaviors of  $\text{Mn}_3\text{O}_4$  nanorods have been discussed in terms of the unique cation distribution in the  $\text{Mn}_3\text{O}_4$  structure, the size effects, and the shape of  $\text{Mn}_3\text{O}_4$  nanorods.

## Experimental section

The 30–50 nm  $\text{Mn}_3\text{O}_4$  nanorods used in our work were prepared by a two-phase approach.<sup>33</sup> The first step is to prepare  $\gamma\text{-MnOOH}$  nanorods as a precursor by the hydrothermal method. Then, the  $\gamma\text{-MnOOH}$  nanorods were calcined at 400 °C in argon for 4 h for converting into  $\text{Mn}_3\text{O}_4$  nanorods. The samples were characterized by transmission electron microscopy (TEM) (200 kV, HITACHI, H-8100) and high-resolution transmission electron microscopy (HRTEM) (JEOL JEM-3010). The structural feature of the samples was characterized using X-ray diffraction (MicroMax-007HF, Rigaku, Japan) with Cu K $\alpha$  radiation (wavelength 1.5406 Å). High-pressure studies were performed in a DAC (400  $\mu\text{m}$  culet size, T301 stainless-steel gasket  $\sim 40$   $\mu\text{m}$  thickness, and 110  $\mu\text{m}$  diameter hole). A small number of  $\text{Mn}_3\text{O}_4$  nanorods were loaded in the sample chamber of the DAC along with a small ruby. In order to ensure a quasi-hydrostatic pressure environment, we used a 4 : 1 methanol-ethanol mixture as a pressure transmitting medium. The pressure inside the sample chamber was calibrated by the fluorescence shifts of the ruby. High-pressure XRD experiments were performed at the 16-BMD beamline of the High Pressure Collaborative Access Team (HPCAT) facility, and the 4W2 beamline of the Beijing Synchrotron Radiation Facility (BSRF), with the incident light wavelength at 0.4066 Å. Then the Dioptas software was used to integrate the 2D XRD images, and convert them into 1D diffraction patterns. Rietveld fitting of the XRD patterns was achieved in the GSAS software. High-pressure *in situ* Raman spectra were collected by using a Renishaw inVia Raman Microscope. The samples were excited at 514.5 nm by using an argon ion laser.

## Results and discussion

Fig. 1(a) shows the representative TEM images of the  $\text{Mn}_3\text{O}_4$  nanorods. We can see that all nanorods have a highly uniform size, with the diameter evenly distributed in the range of 30–50 nm. The HRTEM image in Fig. 1(b) demonstrates that the nanorod is a single crystal structure. The measured crystal plane spacing is 0.305 nm, corresponding to the (112) crystal

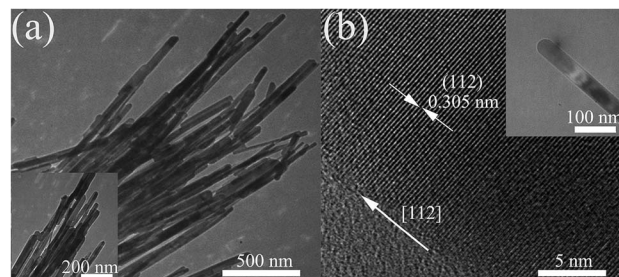


Fig. 1 (a) TEM images of  $\text{Mn}_3\text{O}_4$  nanorods at different magnifications. (b) TEM (the inset) image of a single  $\text{Mn}_3\text{O}_4$  nanorod and the corresponding HRTEM image.

plane of  $\text{Mn}_3\text{O}_4$ , which is perpendicular to the growth direction of the rod, indicating that  $\text{Mn}_3\text{O}_4$  nanorods grow along the [112] direction. The XRD pattern of  $\text{Mn}_3\text{O}_4$  nanorods under ambient conditions also shows that the samples have a hausmannite structure (Fig. S1, ESI†).

The selected high pressure XRD patterns for the  $\text{Mn}_3\text{O}_4$  nanorods up to 42.3 GPa are shown in Fig. 2(a).  $\text{Mn}_3\text{O}_4$  nanorods have a tetragonal structure (hausmannite phase) with a space group  $I4_1/amd$ . At 1.4 GPa, we obtained  $a = b = 5.7574$  (6) Å,  $c = 9.3965$  (4) Å, and  $V = 311.168$  Å<sup>3</sup>; the fitting results are shown in Fig. 2(b). As pressure increased, all diffraction peaks of the initial hausmannite phase move to a higher angle, which indicates the pressure-induced shrinkage of the unit cells. Clearly, the first phase transition starts to occur at  $\sim 15.3$  GPa, with two new diffraction peaks at  $\sim 7.4^\circ$  and  $\sim 9.2^\circ$ . As the pressure increases to 17.2 GPa, a series of new diffraction peaks appear, accompanied by the significant weakening of the diffraction peaks of the initial hausmannite phase. Further increasing pressure to 18.9 GPa, several new diffraction peaks enhanced remarkably, at  $\sim 9.0^\circ$ ,  $\sim 11.2^\circ$  and  $\sim 12.0^\circ$ , which come from the second high pressure phase. Above 22.0 GPa, the diffraction peaks of the first high-pressure phase weaken significantly and even disappear, indicating the second phase transition completion. Obviously,  $\text{Mn}_3\text{O}_4$  nanorods undergo two high-pressure phase transitions during the compression. This is similar to the previously observed phase transitions in  $\text{Mn}_3\text{O}_4$  nanoparticles.<sup>32</sup> The first high-pressure phase was considered in previous studies as an orthorhombic  $\text{CaTi}_2\text{O}_4$ -type structure ( $Bbmm$ ).<sup>32</sup> To determine the second high-pressure phase structure, the orthorhombic marokite structure ( $Pbcm$ ) was used to match the XRD experimental patterns. Fig. 2(c) shows a refinement result of XRD data at 29.6 GPa. Obviously, the second high pressure phase is the marokite-like phase. The cell parameters  $a$ ,  $b$ ,  $c$  and the cell volume  $V$  are assigned to be 2.8746(5) Å, 9.3491(4) Å, 9.2084(9) Å and 247.483 Å<sup>3</sup>, respectively. Fig. 2(a) gives the diffraction pattern of the released  $\text{Mn}_3\text{O}_4$  nanorods at ambient pressure. The refinement result is shown in Fig. S2.† It is noted that the marokite-like phase can be stable under ambient conditions, without the appearance of the hausmannite phase and the orthorhombic phase. The decompression sequence of the  $\text{Mn}_3\text{O}_4$  nanorods is consistent with that of the bulk  $\text{Mn}_3\text{O}_4$ , whereas the coexistence of



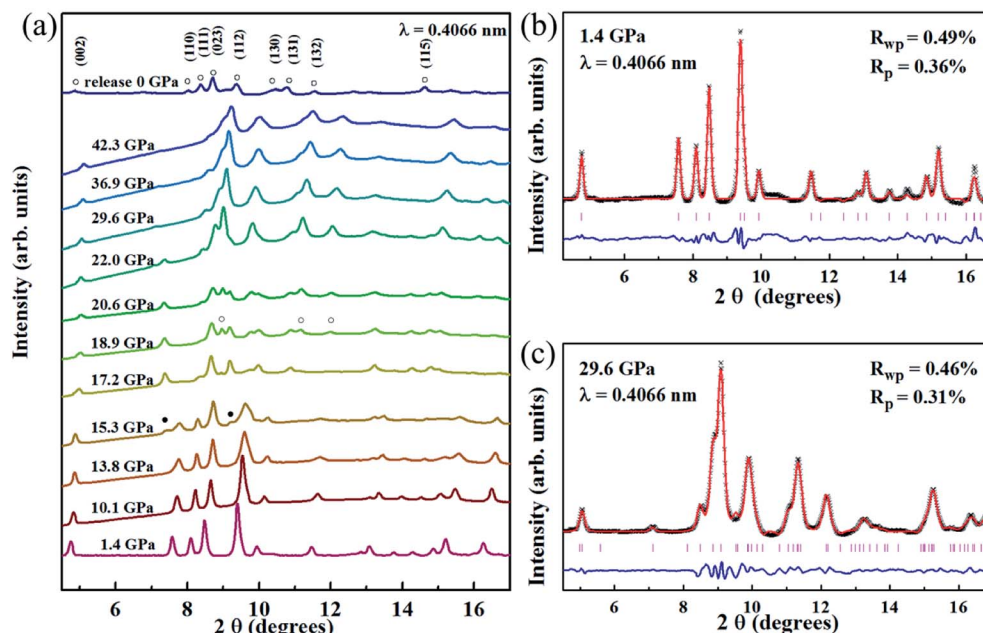


Fig. 2 (a) XRD patterns of Mn<sub>3</sub>O<sub>4</sub> nanorods taken on compression, and unloaded at ambient pressure, in which the solid circle and the hollow circle represent the diffraction peaks of the CaTi<sub>2</sub>O<sub>4</sub>-type structure and the marokite-like phase, respectively. XRD data of the Mn<sub>3</sub>O<sub>4</sub> nanorods at (b) 1.4 GPa and (c) 29.6 GPa were refined. Red solid curve is the result of the Rietveld refinement with the (b) hausmannite phase (*I4<sub>1</sub>/amd*) and (c) marokite-like phase (*Pbcm*) model.

hausmannite and marokite phases was observed in the recovered Mn<sub>3</sub>O<sub>4</sub> nanoparticles.<sup>32</sup> The unusual decompression behaviors of Mn<sub>3</sub>O<sub>4</sub> are similar to the CdS. Previous studies on CdS have found that the shape of nanomaterials plays a crucial role in determining the reversibility of phase transitions.<sup>34</sup> Similarly, the different decompression behaviors between the Mn<sub>3</sub>O<sub>4</sub> nanorods and Mn<sub>3</sub>O<sub>4</sub> nanoparticles are also caused by the shape of Mn<sub>3</sub>O<sub>4</sub>.

In order to confirm the phase transition, we also implemented an *in situ* Raman study on Mn<sub>3</sub>O<sub>4</sub> nanorods. Fig. 3 gives

the measured Raman data of the Mn<sub>3</sub>O<sub>4</sub> nanorods and the functional relationship between Raman displacement and pressure. In the Raman spectrum at 1.1 GPa, three Raman peaks located at 666, 379 and 325 cm<sup>-1</sup> are observed, which is consistent with the hausmannite Mn<sub>3</sub>O<sub>4</sub> in previous reports.<sup>32,35</sup> The stronger Raman peak at 666 cm<sup>-1</sup> is considered to be the A<sub>1g</sub> mode, which is caused by the stretching vibration of the Mn<sup>2+</sup>-O band. With enhancing pressure to 17.2 GPa, the Raman peak of the hausmannite phase weakens significantly. At the same time, the A<sub>1g</sub> mode begins to show a shoulder shape, with

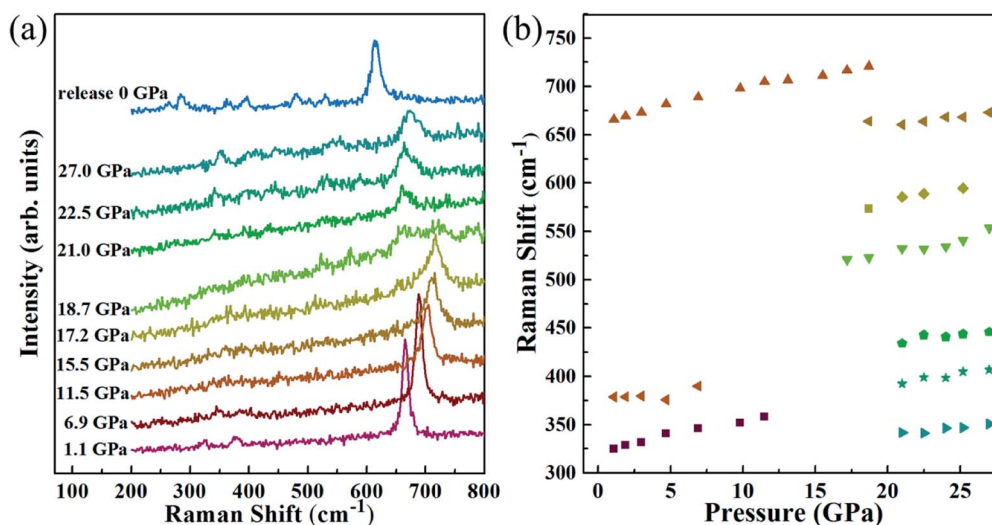


Fig. 3 (a) Raman spectra of Mn<sub>3</sub>O<sub>4</sub> nanorods under high pressure, (b) pressure dependence of Raman modes.



a new Raman peak at  $\sim 655\text{ cm}^{-1}$ . Additionally, two extra Raman peaks in the range of  $500\text{--}660\text{ cm}^{-1}$  appear above this pressure. This indicates that a structural phase transition occurs. Above  $21.0\text{ GPa}$ , the  $A_{1g}$  mode starts to disappear and three additional Raman modes appear within  $300\text{--}450\text{ cm}^{-1}$ , indicating that the second phase transition occurs. We found that all the Raman modes above  $17.2\text{ GPa}$  belong to the marokite-like phase, and the Raman modes of the first high-pressure phase are not observed. This may be caused by the absence of the Raman active mode in the first high-pressure phase. During decompression, the Raman spectra of  $\text{Mn}_3\text{O}_4$  nanorods are shown in Fig. S3.† It is noted that the  $\text{Mn}_3\text{O}_4$  nanorods do not undergo phase transition and remain in the marokite-like phase when the pressure releases. These results are in good agreement with the high-pressure XRD consequences.

Fig. 4 demonstrates the variations of normalized cell parameters and the unit-cell volume for the  $\text{Mn}_3\text{O}_4$  nanorods. From Fig. 4 (a), it is noted that the  $a$  and  $c$  axes show a significant compressional anisotropy. Between  $0$  and  $8.3\text{ GPa}$ , the cell parameters  $a$  and  $c$  for the  $\text{Mn}_3\text{O}_4$  nanorods are reduced by  $1.3\%$  and  $2.5\%$ , respectively. The  $c$  axis is more compressible than the  $a$  axis, which can be interpreted by the structure of hausmannite  $\text{Mn}_3\text{O}_4$  that  $\text{MnO}_6$  octahedra are stretched along the  $[001]$  orientation. In previous studies, the cell parameters  $a$  and  $c$  decreased by  $1.4\%$  and  $2.1\%$  for bulk  $\text{Mn}_3\text{O}_4$  ( $0.9\%$  and  $2.1\%$  for the  $\text{Mn}_3\text{O}_4$  nanoparticles), respectively.<sup>32</sup> Compared with bulk  $\text{Mn}_3\text{O}_4$ , the  $c$  axis of the  $\text{Mn}_3\text{O}_4$  nanorods and nanoparticles both show higher compressibility than the  $a$  axis. Obviously, the nanosize-effects influence the compressibility of  $\text{Mn}_3\text{O}_4$ . The Jahn–Teller distortion in  $\text{Mn}_3\text{O}_4$  has been described in previous

reports as a tetragonal distortion ( $c/2^{1/2}a$ ), which is considered to be an important factor in driving the phase transition.<sup>36</sup> In our study, the tetragonal distortion ( $c/2^{1/2}a$ ) decreases with pressure from  $1.162$  at  $0\text{ GPa}$  to  $1.148$  at  $8.3\text{ GPa}$ , which demonstrates that the Jahn–Teller distortion of  $\text{MnO}_6$  octahedra is suppressed.<sup>36</sup> However, it has been reported that this parameter decreases from  $1.164$  to  $1.150$  in the range of  $0\text{--}8.6\text{ GPa}$  for the  $\text{Mn}_3\text{O}_4$  nanoparticles (decreases from  $1.163$  to  $1.155$  for the bulk  $\text{Mn}_3\text{O}_4$ ).<sup>32</sup> Similar to  $\text{Mn}_3\text{O}_4$  nanoparticles, the decrease of the tetragonal distortion parameter in  $\text{Mn}_3\text{O}_4$  nanorods is much larger than in bulk  $\text{Mn}_3\text{O}_4$ . We believe that the suppressed tetragonal distortion inhibits the transformation from the hausmannite to marokite-like phases, which may be a possible factor for the appearance of the  $\text{CaTi}_2\text{O}_4$ -type structure. Between  $22.0\text{ GPa}$  and  $42.3\text{ GPa}$ , the  $a$  and  $c$  axes exhibit very similar compressibility, which may be caused by the significantly decreased elongation of  $\text{MnO}_6$  octahedra along the  $[001]$  direction with increasing pressure. Therefore, the compressional anisotropy between  $a$  and  $c$  axes almost disappears in the marokite-like phase.

The volume variation of  $\text{Mn}_3\text{O}_4$  nanorods is shown in Fig. 4(b). And then the Birch–Murnaghan equation of state was used to fit the bulk modulus ( $B_0$ ). We selected a certain value of  $4$  ( $B_0'$ ) for the calculation of the bulk modulus. From  $1.4$  to  $15.3\text{ GPa}$ ,  $\text{Mn}_3\text{O}_4$  nanorods are in the initial hausmannite phase. The fitted result shows that the bulk modulus ( $B_0$ ) obtained is  $154 \pm 5.5\text{ GPa}$ . Between  $22.0$  and  $42.3\text{ GPa}$ , the  $\text{Mn}_3\text{O}_4$  nanorods are in the marokite-like phase and the bulk modulus obtained is  $176 \pm 7.7\text{ GPa}$ . Compared with the hausmannite phase, the bulk modulus of the marokite-like structure is

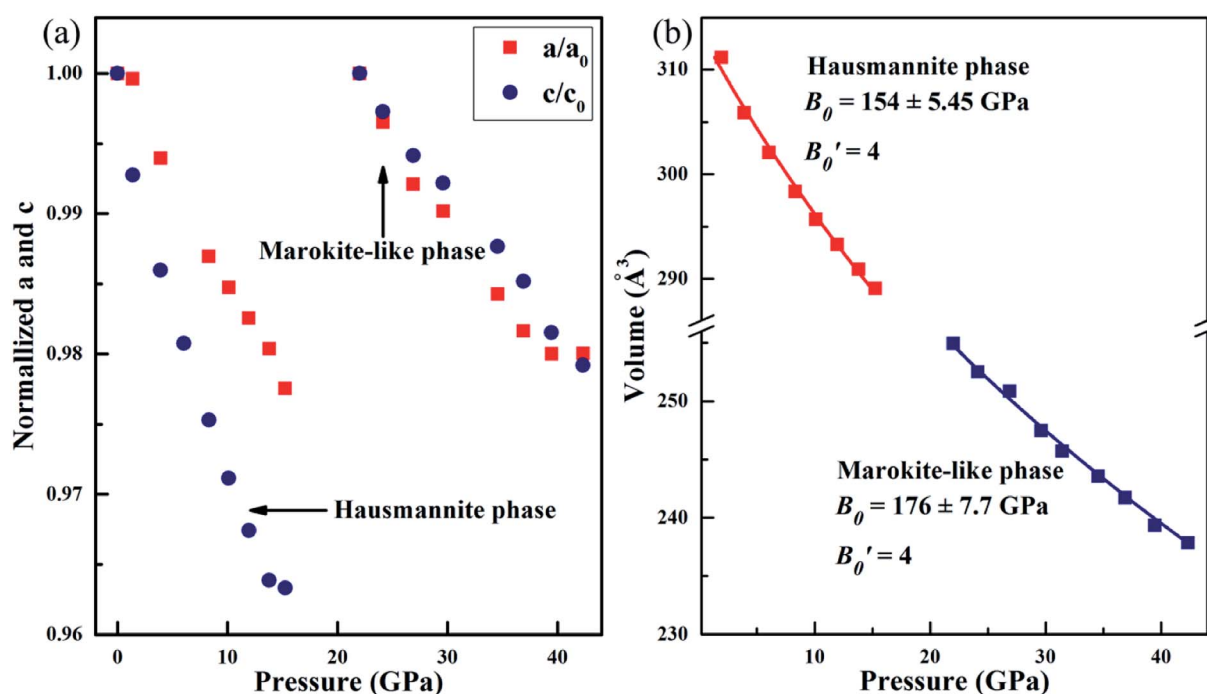


Fig. 4 (a) Variation of lattice parameters  $a$  and  $c$  with pressure after normalization treatment. (b) Unit-cell volume of  $\text{Mn}_3\text{O}_4$  nanorods as a function of pressure.





significantly larger. Therefore, the compressibility of the marokite-like phase is lower than the hausmannite phase. It was known that the bulk moduli of the hausmannite phase  $\text{Mn}_3\text{O}_4$  bulk and nanoparticles are  $168 \pm 18.3$  GPa and  $202 \pm 6$  GPa, respectively.<sup>32</sup> The bulk modulus of the  $\text{Mn}_3\text{O}_4$  nanorods approaches that of the corresponding bulk, but much less than that of nanoparticles. Clearly, the bulk modulus in the hausmannite phase shows a shape-tuned feature. The  $\text{Mn}_3\text{O}_4$  nanorods are more compressible than nanoparticles and bulk counterparts. A similar behavior has been also observed in  $\text{TiO}_2$  anatase nanoparticles, in which the bulk modulus of the rod-shaped  $\text{TiO}_2$  is significantly smaller than the bulk counterpart before phase transition.<sup>20</sup> The author suggested that this may be attributed to the differences in the number of soft empty oxygen octahedral units in different crystals, the anisotropic distribution of crystal chemical defects, and the dependence on the size and morphology.<sup>20</sup> But in the CdS nanorods<sup>34</sup> and ZnO nanowires,<sup>37</sup> the bulk moduli of the CdS nanorods and ZnO nanowires are dramatically larger than their bulk counterparts. In the report of CdS, it has been revealed that the differences in the bulk modulus are caused by the different morphologies.<sup>34</sup> However, in the study on ZnO nanowires, the author has proposed that the high crystallinity and defect-free nature of the nanowires are the main reasons that cause the enhancement of mechanical properties.<sup>37</sup> Therefore, there is still no consensus on how the morphology affects the value of bulk modulus, and more detailed and comprehensive studies on nanomaterials with varying shapes are necessary to better understand these findings.

To determine the morphology of the  $\text{Mn}_3\text{O}_4$  nanorods after compression, the TEM and HRTEM images of the samples after being unloaded from 42.0 GPa are shown in Fig. 5(a) and (b), respectively. It is clear that the long  $\text{Mn}_3\text{O}_4$  nanorods are crushed into some short nanorods, which may be caused by the non-hydrostatic pressure conditions and the phase transitions under high pressure. The HRTEM image shows that the measured crystal plane spacing is 0.217 nm for the nanorods, corresponding to the (130) plane of the marokite-like phase  $\text{Mn}_3\text{O}_4$ .

Here we discuss the possible reason for the high-pressure behaviors in  $\text{Mn}_3\text{O}_4$  nanorods. Previous studies on  $\text{Mn}_3\text{O}_4$

suggested that the suppressed Jahn–Teller distortion, the structure deformation together with the decrease of volume are the main factors driving the structure transitions.<sup>36</sup> Other reports have revealed that the  $\text{Mn}^{3+}/\text{Mn}^{2+}$  ratio of the hausmannite phase nanomaterials is slightly lower than that of the bulk counterpart, indicating that the cation distribution in nanomaterials is different.<sup>38,39</sup> Furthermore, the local stresses within the nanodomain structure and the cation inversion may lower the Jahn–Teller distortion of the  $\text{AB}_2\text{O}_4$  formula compounds.<sup>40</sup> In our case, we prefer the suppressed Jahn–Teller distortion, the nanosize effects and the shape-dependence as the primary reasons for the unusual phase transition behavior of the  $\text{Mn}_3\text{O}_4$  nanorods. The phase transition pathway of the  $\text{Mn}_3\text{O}_4$  nanorods during the pressurization is consistent with that of  $\text{Mn}_3\text{O}_4$  nanoparticles and significantly different from that of bulk counterparts, which may be caused by the nanosize effects and the cation distribution in the  $\text{Mn}_3\text{O}_4$  nanorods. Moreover, compared with the bulk counterpart, the Jahn–Teller distortion parameters of the  $\text{Mn}_3\text{O}_4$  nanorods and nanoparticles show a significant decrease upon compression. Therefore, the suppressed Jahn–Teller distortion is also a possible factor for the new phase (orthorhombic  $\text{CaTi}_2\text{O}_4$ -type structure) appearance. However, compared with  $\text{Mn}_3\text{O}_4$  nanoparticles, the increase of the phase transition pressure, the smaller bulk modulus and the different decompression behavior observed in the  $\text{Mn}_3\text{O}_4$  nanorods can be attributed to the influences of their rod-shape and growth orientation. The similar morphology influences on the bulk modulus and decompression behavior have also been observed in CdS nanorods.<sup>34</sup> Based on the above discussions, we believe that our study offers a reference for better understanding the influences of the size and morphology on the behaviors of the  $\text{Mn}_3\text{O}_4$  nanorods under high pressure.

## Conclusions

In summary, we have performed *in situ* XRD and Raman scattering to investigate the high-pressure behaviors of  $\text{Mn}_3\text{O}_4$  nanorods. It was found that the  $\text{Mn}_3\text{O}_4$  nanorods show a similar phase transition routine with the  $\text{Mn}_3\text{O}_4$  nanoparticles and undergo two phase transitions: from the hausmannite phase to the orthorhombic  $\text{CaTi}_2\text{O}_4$ -type structure at  $\sim 15.3$  GPa, then to the marokite-like phase at  $\sim 18.9$  GPa. This is different from the direct transformation from the hausmannite to marokite phase at  $\sim 11.5$  GPa observed in bulk  $\text{Mn}_3\text{O}_4$ .<sup>32</sup> The difference in the phase transition routine results from nanosize effects and the suppressed Jahn–Teller distortion. Compared with the corresponding  $\text{Mn}_3\text{O}_4$  nanoparticles and the bulk counterparts, hausmannite phase  $\text{Mn}_3\text{O}_4$  nanorods show a better stability with the first phase transition at  $\sim 15.3$  GPa and a smaller bulk modulus. It is proposed that the nanorod shape makes it more compressible. In addition, the *c* axis of the  $\text{Mn}_3\text{O}_4$  nanorods shows higher compressibility than the *a* axis, which is similar to the  $\text{Mn}_3\text{O}_4$  nanoparticles. We propose that this phenomenon results from the stretching of

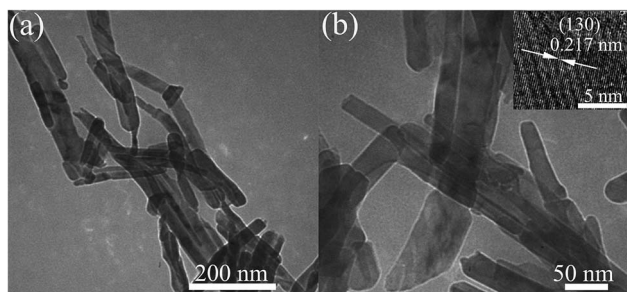


Fig. 5 (a) TEM image of the  $\text{Mn}_3\text{O}_4$  nanorods after being released from 42.0 GPa. (b) TEM with higher magnification and the corresponding HRTEM image.



the  $\text{MnO}_6$  octahedra along the [001] orientation and the nanosize effects. While upon decompression to the atmospheric pressure, the  $\text{Mn}_3\text{O}_4$  nanorods keep the marokite-like phase, which is consistent with that of the bulk  $\text{Mn}_3\text{O}_4$ , whereas the coexistence of hausmannite and marokite phases is observed in the recovered  $\text{Mn}_3\text{O}_4$  nanoparticles. It is interesting that the  $\text{Mn}_3\text{O}_4$  nanorods show similar phase transition sequences with the nanoparticles upon compression, but retain the high pressure phase like the bulk counterparts. These observations clearly demonstrate that both the shape and the size-effects are crucial factors for the behaviors of the  $\text{Mn}_3\text{O}_4$  nanorods under high pressure. Our study provides better help to fully understand the influences of the morphology and size on the phase transitions of nanomaterials.

## Conflicts of interest

There are no conflicts of interest to declare.

## Acknowledgements

This work was financially supported by the National Key R&D Program of China (No. 2018 YFA0305900), the National Natural Science Foundation of China (11874172, 11374120, 11634004 and 51320105007), and Jilin University Science and Technology Innovative Research Team (2017TD-01).

## References

- H. Wu, Z. Wang and H. Fan, *J. Am. Chem. Soc.*, 2014, **136**, 7634–7636.
- B. Li, K. Bian, X. Zhou, P. Lu, S. Liu, I. Brener, M. Sinclair, T. Luk, H. Schunk, L. Alarid, P. G. Clem, Z. Wang and H. Fan, *Sci. Adv.*, 2017, **3**, 1–8.
- Z. Quan, Z. Luo, Y. Wang, H. Xu, C. Wang, Z. Wang and J. Fang, *Nano Lett.*, 2013, **13**, 3729–3735.
- F. Bai, K. Bian, X. Huang, Z. Wang and H. Fan, *Chem. Rev.*, 2019, **119**, 7673–7717.
- Z. Wang, Y. Zhao, D. Schiferl, J. Qian, R. T. Downs, H. K. Mao and T. Sekine, *J. Phys. Chem. B*, 2003, **107**, 14151–14153.
- J. Zhu, Z. Quan, C. Wang, X. Wen, Y. Jiang, J. Fang, Z. Wang, Y. Zhao and H. Xu, *Nanoscale*, 2016, **8**, 5214–5218.
- Q. Guo, Y. Zhao, W. L. Mao, Z. Wang, Y. Xiong and Y. Xia, *Nano Lett.*, 2008, **8**, 972–975.
- L. Wang, W. Yang, Y. Ding, Y. Ren, S. Xiao, B. Liu, S. V. Sinogeikin, Y. Meng, D. J. Gosztola, G. Shen, R. J. Hemley, W. L. Mao and H. K. Mao, *Phys. Rev. Lett.*, 2010, **105**, 1–4.
- Z. Li, L. Wang, B. Liu, J. Wang, B. Liu, Q. Li, B. Zou, T. Cui, Y. Meng, H. Kwang Mao, Z. Liu and J. Liu, *Phys. Status Solidi B*, 2011, **248**, 1149–1153.
- R. S. Kumar, A. L. Cornelius and M. F. Nicol, *Curr. Appl. Phys.*, 2007, **7**, 135–138.
- G. R. Hearne, J. Zhao, A. M. Dawe, V. Pischedda, M. Maaza, M. K. Nieuwoudt, P. Kibasomba, O. Nemraoui, J. D. Comins and M. J. Witcomb, *Phys. Rev. B: Condens. Matter Mater. Phys.*, 2004, **70**, 1–10.
- B. Liu, B. Liu, M. Yao, Z. Li, R. Liu, Q. Li, D. Li, B. Zou, T. Cui, G. Zou, J. Liu and Z. Chen, *J. Phys. Chem. C*, 2011, **115**, 4546–4551.
- V. Swamy, A. Y. Kuznetsov, L. S. Dubrovinsky, A. Kurnosov and V. B. Prakapenka, *Phys. Rev. Lett.*, 2009, **103**, 1–4.
- L. Q. Huston, A. Lugstein, J. S. Williams and J. E. Bradby, *Appl. Phys. Lett.*, 2018, **12**(113), 123103.
- Y. Lin, Y. Yang, H. Ma, Y. Cui and W. L. Mao, *J. Phys. Chem. C*, 2011, **115**, 9844–9849.
- Z. Dong and Y. Song, *Chem. Phys. Lett.*, 2009, **480**, 90–95.
- Z. Wang, L. L. Daemen, Y. Zhao, C. S. Zha, R. T. Downs, X. Wang, Z. L. Wang and R. J. Hemley, *Nat. Mater.*, 2005, **4**, 922–927.
- T. H. Zhongwu Wang, Xiao-D. Wen, R. Hoffmann, J. S. Son, R. Li, C.-chen Fang and D.-M. Smilgies, *Proc. Natl. Acad. Sci. U. S. A.*, 2017, **1**, 2017.
- Q. Li, B. Liu, L. Wang, D. Li, R. Liu, B. Zou, T. Cui, G. Zou, Y. Meng, H. Kwang Mao, Z. Liu, J. Liu and J. Li, *J. Phys. Chem. Lett.*, 2010, **1**, 309–314.
- S. W. Park, J. T. Jang, J. Cheon, H. H. Lee, D. R. Lee and Y. Lee, *J. Phys. Chem. C*, 2008, **112**, 9627–9631.
- L. Wang, H. Liu, J. Qian, W. Yang and Y. Zhao, *J. Phys. Chem. C*, 2012, **116**, 2074–2079.
- Q. Li, W. Niu, X. Liu, Y. Chen, X. Wu, X. Wen, Z. Wang, H. Zhang and Z. Quan, *J. Am. Chem. Soc.*, 2018, **140**, 15783–15790.
- V. Swamy, A. Kuznetsov, L. S. Dubrovinsky, R. A. Caruso, D. G. Shchukin and B. C. Muddle, *Phys. Rev. B: Condens. Matter Mater. Phys.*, 2005, **71**, 15–17.
- Q. Li, B. Cheng, X. Yang, R. Liu, B. Liu, J. Liu, Z. Chen, B. Zou, T. Cui and B. Liu, *J. Phys. Chem. C*, 2013, **117**, 8516–8521.
- Z. Li, B. Liu, S. Yu, J. Wang, Q. Li, B. Zou, T. Cui, Z. Liu, Z. Chen and J. Liu, *J. Phys. Chem. C*, 2011, **115**, 357–361.
- V. Swamy, A. Kuznetsov, L. S. Dubrovinsky, P. F. McMillan, V. B. Prakapenka, G. Shen and B. C. Muddle, *Phys. Rev. Lett.*, 2006, **96**, 19–21.
- Y. Wang, J. Zhu, W. Yang, T. Wen, M. Pravica, Z. Liu, M. Hou, Y. Fei, L. Kang, Z. Lin, C. Jin and Y. Zhao, *Nat. Commun.*, 2016, **7**, 1–8.
- L. Zhang, Q. Zhou, Z. Liu, X. Hou, Y. Li and Y. Lv, *Chem. Mater.*, 2009, **21**, 5066–5071.
- A. Vázquez-Olmos, R. Redón, G. Rodríguez-Gattorno, M. E. Mata-Zamora, F. Morales-Leal, A. L. Fernández-Osorio and J. M. Saniger, *J. Colloid Interface Sci.*, 2005, **291**, 175–180.
- Z. Wang, S. K. Saxena and C. S. Zha, *Phys. Rev. B: Condens. Matter Mater. Phys.*, 2002, **66**, 241031–241036.
- B. N. Kim, K. Hiraga, K. Morita and Y. Sakka, *Nature*, 2001, **413**, 288–291.
- H. Lv, M. Yao, Q. Li, Z. Li, B. Liu, R. Liu, S. Lu, D. Li, J. Mao, X. Ji, J. Liu, Z. Chen, B. Zou, T. Cui and B. Liu, *J. Phys. Chem. C*, 2012, **116**, 2165–2171.
- L. Lan, Q. Li, G. Gu, H. Zhang and B. Liu, *J. Alloys Compd.*, 2015, **644**, 430–437.



- 34 L. Meng, J. M. D. Lane, L. Baca, J. Tafoya, T. Ao, B. Stoltzfus, M. Knudson, D. Morgan, K. Austin, C. Park, P. Chow, Y. Xiao, R. Li, Y. Qin and H. Fan, *J. Am. Chem. Soc.*, 2020, **142**, 6505–6510.
- 35 X. J. Liu, S. Xu, K. Kato and Y. Moritomo, *J. Phys. Soc. Jpn.*, 2002, **71**, 2820–2821.
- 36 Y. Moritomo, Y. Ohishi, A. Kuriki, E. Nishibori, M. Takata and M. Sakata, *J. Phys. Soc. Jpn.*, 2003, **72**, 765–766.
- 37 Z. Dong, K. K. Zhuravlev, S. A. Morin, L. Li, S. Jin and Y. Song, *J. Phys. Chem. C*, 2012, **116**, 2102–2107.
- 38 L. Laffont and P. Gibot, *Mater. Charact.*, 2010, **61**, 1268–1273.
- 39 J. Kaczmarek and E. Wolska, *J. Solid State Chem.*, 1993, **103**, 387–393.
- 40 Y. M. Chiang, H. Wang and Y. I. Jang, *Chem. Mater.*, 2001, **13**, 53–63.

